ADVANCED SCIENCE Open Access
www.advancedscience.com

Cyclic Arginine–Glycine–Aspartate-Decorated Lipid Nanoparticle Targeting toward Inflammatory Lesions Involves Hitchhiking with Phagocytes

Alexandros Marios Sofias, Geir Bjørkøy, Jordi Ochando, Linda Sønstevold, Maria Hegvik, Catharina de Lange Davies, Olav Haraldseth, Twan Lammers, Willem J. M. Mulder, and Sjoerd Hak**

Active-targeting nanomedicine formulations have an intricate in vivo behavior. Nanomedicines developed to target endothelial $\alpha_v\beta_3$-integrin are recently demonstrated to display extensive uptake by circulating phagocytes. These phagocytes show inherent tumor-homing capacities and therefore are capable of actively delivering the endocytosed nanomaterial in lesions. Here, the targeting kinetics and mechanisms of cyclic arginine–glycine–aspartate (cRGD)-decorated lipid nanoparticles (NPs) toward activated vasculature in inflamed lesions during wound healing are studied. The cRGD-NP targeting toward inflamed lesions is identified to be mechanistically similar to the NP accumulation in cancerous lesions. Through a complementary experimental approach, it is observed that circulating phagocytes engage cRGD-NPs and are subsequently homed to the inflamed endothelium. The inflammation-associated phagocytes remain static among endothelial cells upon targeting, resulting in the extensive presence of cRGD-NP-positive phagocytes in the angiogenic vessels. Hence, phagocytic immune cells contribute to cRGD-NP targeting toward angiogenesis. This mechanistic study underlines the need for detailed investigations of NP in vivo behavior. This is critically important for the realization of NPs potential as advanced (immunological) therapeutic agents.

1. Introduction

Recent research on active-targeting nanomedicines has revealed an intricate in vivo behavior of these agents that goes beyond the conventional notion of receptor-targeting. Various ligand-decorated nanoparticles (NPs) show elevated uptake into phagocytes and this propensity has also been utilized for therapeutic phagocyte targeting.[1,2] Targeting the various subpopulations of the immune system with NPs, offers many possibilities. NPs can target myeloid or lymphoid cells delivering immunotherapeutic payload that can polarize phagocytes to an antitumor phenotype[3] and can improve the immunological antitumor responses.[1] In addition, given the propensity of the immune cells to migrate in diseased and cancerous lesions, targeting immune cells with NPs offers the possibility to use these cells as indirect drug delivery vehicles.[4]

Dr. A. M. Sofias, L. Sønstevold, M. Hegvik, Prof. O. Haraldseth, Dr. S. Hak
Department of Circulation and Medical Imaging
Faculty of Medicine and Health Sciences
Norwegian University of Science and Technology (NTNU)
Trondheim 7030, Norway
E-mail: alexandros.m.sofias@ntnu.no; asofias@ukaachen.de; sjoerd.hak@ntnu.no; sjoerd.hak@sintef.no

Dr. A. M. Sofias, Prof. W. J. M. Mulder
BioMedical Engineering and Imaging Institute
Icahn School of Medicine at Mount Sinai
New York, NY 10029, USA

The ORCID identification number(s) for the author(s) of this article can be found under https://doi.org/10.1002/advs.202100370

DOI: 10.1002/advs.202100370

Dr. A. M. Sofias, Prof. T. Lammers
Department of Nanomedicine and Theranostics
Institute for Experimental Molecular Imaging
RWTH Aachen University
Aachen 52074, Germany

Prof. G. Bjørkøy
Department of Clinical and Molecular Medicine
Faculty of Medicine and Health Sciences
Norwegian University of Science and Technology (NTNU)
Trondheim 7030, Norway

Prof. G. Bjørkøy
Department of Biomedical Laboratory Science
Faculty of Natural Sciences
Norwegian University of Science and Technology (NTNU)
Trondheim 7030, Norway

Prof. G. Bjørkøy
Centre of Molecular Inflammation Research (CEMIR)
Faculty of Medicine and Health Sciences
Norwegian University of Science and Technology (NTNU)
Trondheim 7030, Norway

We previously demonstrated that NP decoration with cyclic arginine–glycine–aspartate (cRGD) peptides, developed and widely used and clinically tested to direct NPs toward activated endothelium, results in high engagement of these intravenously injected NPs with myeloid phagocytic immune cells (predominantly neutrophils) in circulation.[5] Moreover, a significant portion of cRGD-NP accumulation in cancerous[6] and inflamed brain[7] lesions occurs via phagocyte hitchhiking. These important realizations have been expanded beyond cancer, since multiple diseases or conditions also appeared to have a particular immunological signature.[8–11] Among these conditions, post-injury inflammation looks extremely appealing as neutrophils, one of the major populations targeted by cRGD-NPs, is a key population in acute inflammation.[12]

The immune cell infiltration and presence in the inflamed or tumor microenvironment is a biologically known phenomenon. Nevertheless, for advancing modern nanoimmunotherapeutics toward clinical translation, quantitative and highly complementary methodologies that can visualize and track NPs at different levels of spatiotemporal resolution are essential for unraveling complex targeting mechanisms and interactions between NPs and immune cells.[13–16]

As such we hereby employed real-time intravital microscopy (IVM) and further supported our observations with ex vivo microscopy and flow cytometry for investigating the kinetics of cRGD-NPs (liposome [LP] and nanoemulsion [NE]; FigureS1, Supporting Information) in an acute wound-derived inflammation model in mice. We identified cRGD-NPs-positive phagocytes to home to the activated endothelium in close proximity to the wound. This behavior resembles the strong NP-neutrophil involvement observed in tumor targeting; interestingly, targeting to the inflamed lesion was found to be more organized as compared to the chaotic immune cell migration that was observed in tumors.

Prof. J. Ochando
Department of Oncological Sciences
Icahn School of Medicine at Mount Sinai
New York, NY 10029, USA
Prof. J. Ochando
Transplant Immunology Unit
National Center of Microbiology
Instituto de Salud Carlos III
Madrid 28220, Spain
Prof. C. de L. Davies
Department of Physics
Norwegian University of Science and Technology (NTNU)
Trondheim 7034, Norway
Prof. T. Lammers
Department of Pharmaceutics
Utrecht Institute for Pharmaceutical Sciences
Utrecht University
Utrecht 3584 CG, The Netherlands
Prof. T. Lammers
Department of Targeted Therapeutics
MIRA Institute for Biomedical Technology and Technical Medicine
University of Twente
Enschede 7522 NB, The Netherlands
Prof. W. J. M. Mulder
Laboratory of Chemical Biology
Department of Biochemical Engineering
Eindhoven University of Technology
Eindhoven 5612 AP, The Netherlands
Dr. S. Hak
Department of Biotechnology and Nanomedicine
SINTEF Industry
Trondheim 7034, Norway

2. Results and Discussion

To study cRGD-NE targeting toward angiogenic endothelium in the inflamed lesions at the cellular level in vivo, we utilized IVM. We induced inflammation in mouse ears by inflicting a small wound.[17,18] Wound healing involves extensive angiogenesis during the first days,[19] and the thin skin of the mouse ear permits IVM of the vasculature. 2 days after inflicting the wound, we dynamically imaged angiogenic vasculature upon intravenous (i.v.) NE administration for half an hour with a temporal resolution of 1 min. In case of cRGD-NE, we observed 1–8 µm-sized cRGD-NE agglomerates which bound and were slowly moving along the blood vessel wall, in a similar fashion as immune cells do (Movie S1, Supporting Information). Interestingly, the observed agglomerates had a ring-like appearance or were associated with immune cell-sized "black holes" (**Figure 1**a–c). Since typically the signal from circulating material is absent inside circulating cells, these black holes were presumably circulating leukocytes. This indicated these cRGD-NE agglomerates to be cell-associated material. Additionally, we observed 1–8 µm-sized cRGD-NE agglomerates that bound to the blood vessel wall and remained stationary (Figure 1d and Movie S2, Supporting Information). In fluorescence versus time plots, these binding events appeared as "steps" (Figure 1d). In case of cRAD-NE, we observed the expected vascular extravasation (Figure 1e and Movie S3, Supporting Information), which is an effect of increased permeability of angiogenic vasculature.[20] Fluorescence versus time plots illustrated the gradual nature of passive accumulation of the cRAD-NE at the angiogenic sites (Figure 1e). When the obtained curves of individual targeting events were averaged, an apparent "s-curve" fluctuation in the targeting rate of cRGD-NE was appreciated (Figure 1f). Interestingly, this fluctuation was similar to the fluctuating cRGD-NE targeting rates toward angiogenic tumor tissue observed with dynamic MRI (Figure 1g)[21] and with IVM[6] in two of our earlier studies. Comparing MRI and IVM dynamic data is obviously not trivial. The clearest difference between the curves was observed in the first 1–2 min post-injection. In the dynamic MRI, the NEs were i.v. injected during imaging and hence the wash-in of the material was detected. In case of IVM, before dynamic imaging was started, receiver gain and laser power needed to be adjusted after NE administration to avoid under- and over-exposure. Hence, the IVM imaging sequence starts after the wash-in has occurred. Furthermore, the efficiency by which MR contrast agents generate image contrast (by altering water proton relaxation times) depends amongst others on their water accessibility. Since compartmentalization upon cellular uptake reduces water accessibility, this will affect signal intensity.[22,23] For fluorophores, cellular internalization may result in changes in the chemical environment or high local fluorophore concentration, which both affect fluorophore brightness. Hence, the signal intensities represent NE concentrations only semi-quantitatively and an exact reproduction of such curves with two different imaging modalities in two different animal models is unlikely. Nevertheless, the

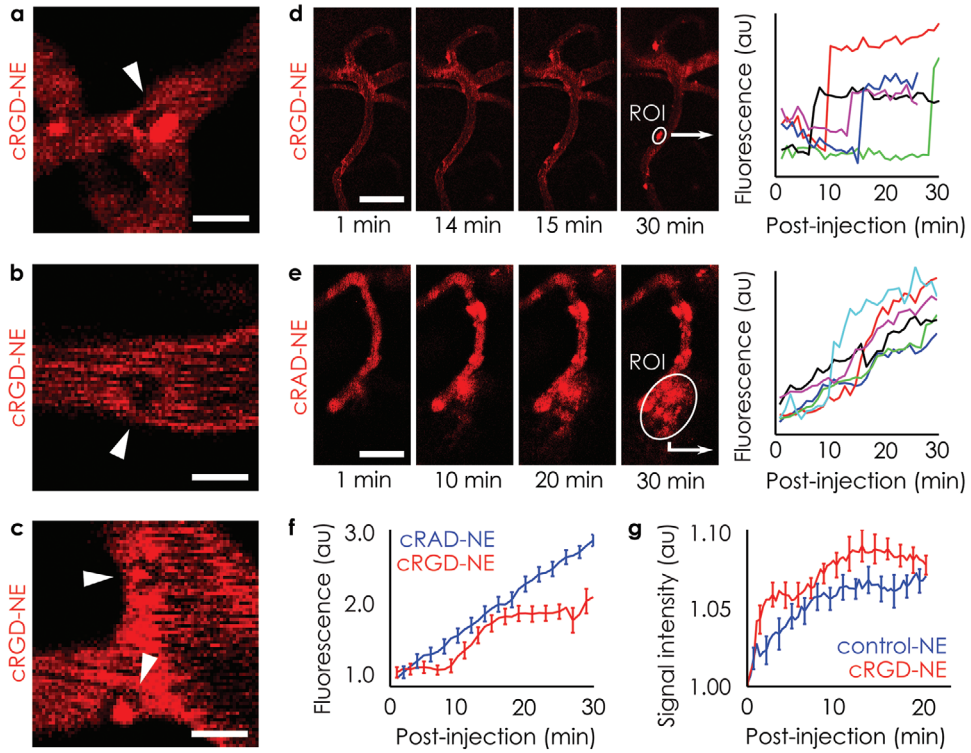

Figure 1. In vivo targeting kinetics studied with dynamic IVM. a–c) Snapshots and enlargements of Movie S1, Supporting Information, showing ring-like cRGD-NE agglomerates (a), as well as cRGD-NE agglomerates associated with circulating "black holes" (b,c). The rings and the "black holes" (indicated with arrowheads) were circular in shape with a diameter of 6–8 μm, which corresponds to the size of circulating neutrophils. d) Snapshots of a dynamic imaging series show binding events in angiogenic vasculature of 1–8 μm-sized cRGD-NE (red) agglomerates, appearing as "steps" in fluorescence versus time plots (each line represents the ROI signal intensity of a single binding event). e) cRAD-NE (red) extravasated gradually in the inflamed tissue. f) The averaged signal as a function of time for cRGD-NE ($n = 4$, 45 binding events) and cRAD-NE ($n = 3$). g) Targeting kinetics in angiogenic tumor tissue, observed with dynamic MRI in an earlier study ($\Delta t = 21$ s; $n = 4$ for each curve, Adapted with permission[21]). Scale bars: a–c = 10 μm; d,e = 50 μm. Error bars: f,g = SEM.

similarities in fluctuating targeting rates observed in the current study with IVM and in previous studies in cancer with both IVM and DCE-MRI may indicate the involvement of similar cRGD-NP targeting mechanisms in cancerous and inflammatory lesions.

To investigate the observed cRGD-NE agglomerates in more detail, we performed high-speed dynamic IVM with temporal resolutions of 0.3–2 s. This allowed for the visualization of fast moving cRGD-NE agglomerates, which showed a striking resemblance to immune cells (Movie S4, Supporting Information). We observed an abundant presence of cRGD-NE positive leukocytes circulating, as well as binding to and rolling along vessel walls as early as 45 min post-injection (**Figure 2**a and Movie S4, Supporting Information). cRAD-NE was also taken up by circulating cells at 45 min post-injection, however, to much lower extent (Movie S5, Supporting Information). This difference was especially apparent after co-injection of cRGD-NE and cRAD-NE, labeled with spectrally different fluorophores, which revealed circulating cells taking up either only cRGD-NE or both cRGD- and cRAD-NE (Figure 2b). 1 h post-injection, we confirmed extensive accumulation of cRGD-NE positive agglomerates in angiogenic vasculature adjacent to the wound (Figure 2b). In mice co-injected with cRGD-NE and cRAD-NE, several of the accumulated cRGD-NE agglomerates also contained some cRAD-NE (Figure 2b). Utilizing TIE2-green fluorescent protein (GFP) mice, which express GFP in vascular endothelial cells, we also detected the expected direct cRGD-NE targeting toward endothelial cells, which was especially apparent at 24 h post-injection (Figure 2c). Z-stacks of regions with targeting revealed cRGD-NE colocalizing with GFP, presumably a result of direct association of NPs with GFP positive endothelium (Figure 2d). Furthermore, we confirmed the presence of non-endothelial cell-sized agglomerates associated with vascular endothelium up to 24 h after cRGD-NE administration (Figure 2d). Expected cRAD-NE extravasation was observed at later time points as well (Figure 2e).

To confirm that the observed agglomerates were immune cells, we obtained blood samples at 5, 10, and 25 min post-co-injection of cRGD-NE and cRAD-NE and isolated white cells using density gradients. Confocal laser scanning microscopy (CLSM) on these isolated cells demonstrated significant association of cRGD-NE with these cells as early as 5 min post-injection (**Figure 3**a) which increased at later time points post-injection (Figure S2, Supporting Information). cRAD-NE also associated with white cells, but to much lower extent (Figure 3a and Figure S2, Supporting Information). Interestingly, z-stacks obtained at these early time points post-injection indicated that cRGD-NE colocalized in many instances with cell surfaces, resulting in ring-like fluorescence signals (Figure 3b,c), which we also observed in vivo (Figure 1a). At 10 (Figure S2, Supporting Information) and 25 min (Figures S2

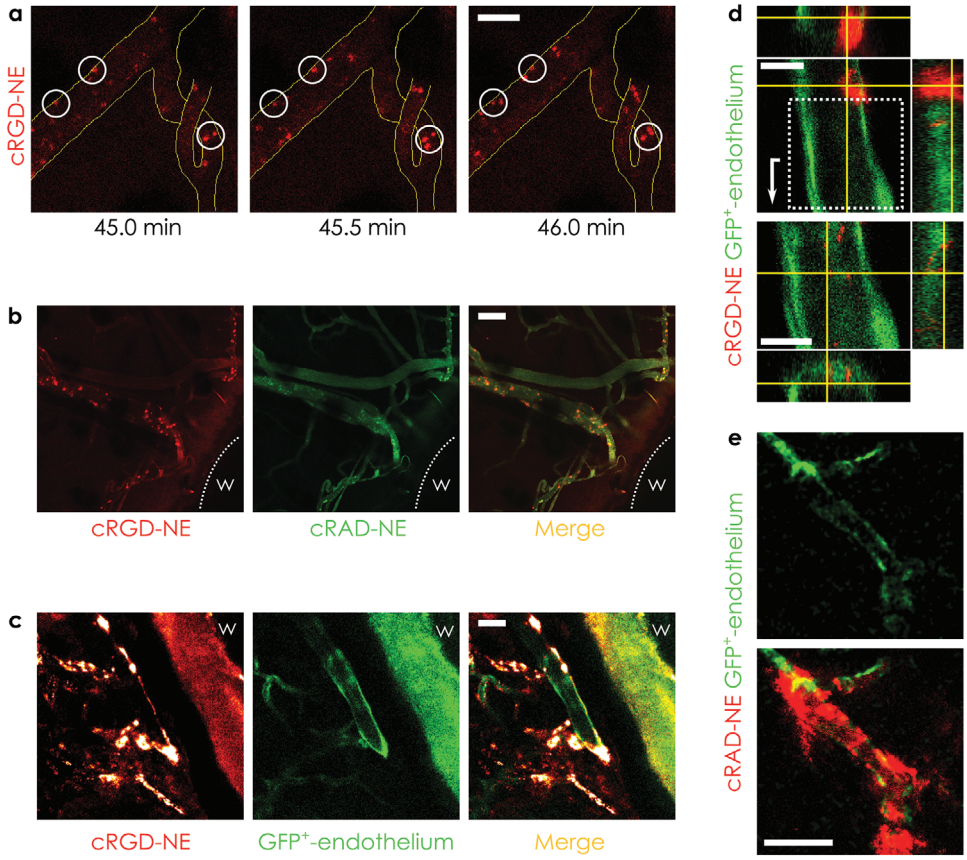

Figure 2. Nanoemulsion association with immune cells and angiogenic tissue. a) High-speed imaging (Δt = 1.3 s) revealed both bound (white circles) and circulating cRGD-NE (red) positive cells (blood vessels delineated in yellow). b) cRGD-NE (Atto633-PE; red) accumulated extensively in cell-sized agglomerates in angiogenic vasculature adjacent to the wound (w) at 1 h post-injection. Several of these aggregates were also positive for co-injected cRAD-NE (Rhodamine-PE; green). c) cRGD-NE (red-hot look-up table to visualize colocalization with GFP) colocalizing with GFP positive endothelium (green) next to the wound (w). d) Z-stack with orthogonal projections showed non-endothelial cRGD-NE cell-sized agglomerates up to 24 h post-injection in the angiogenic vasculature (endothelial GFP; green). When cRGD-NE signal was enhanced (white box enlarged and enhanced), cRGD-NE colocalization with endothelium became evident. e) cRAD-NE (red) predominantly accumulated through passive diffusion from the vasculature (endothelial GFP; green), 1 h post-injection. Scale bars: b,c = 100 µm; a,e = 50 µm; d = 10 µm.

and S3, Supporting Information) post-injection the majority of cell-associated NE was internalized.

To more quantitatively assess the NE internalization by circulating immune cells, we performed flow cytometry on blood cells obtained 2 h after NE administration. To detect the main circulatory immune cell populations, we used FCS/SSC and an antibody panel (consisting of antibodies against CD11b, Ly6G, CD19, and CD3e) allowing us to detect myeloid (neutrophils, M1, and M2 monocytes) and lymphoid (B-cells and T-cells) populations. Figure S4, Supporting Information, outlines our gating strategy. The abundancies of the different cell populations in our set-up resemble closely reported values in literature for Balb/c strain,[24] with neutrophils to be at around 38.6%, monocytes 4.7%, and lymphocytes 56.7%. For sorting M1 and M2 monocytes, one needs typically to use in addition antibodies against F4/80 and Ly6C. Nevertheless, as we have previously shown, these two populations can be separated at earlier stage of the gating strategy by capitalizing on their differences in Ly6G expression, FSC, and SSC.[5] As such, M1 monocytes can be gated as $CD11b^{+}Ly6G^{-}SSC^{low}$ and M2 monocytes as $CD11b^{+}Ly6G^{int}SSC^{high}$. With respect to the NP uptake, we observed the non-phagocytic lymphoid-derived cells (T cells and B cells) to display little interaction with the NE (Figure S5, Supporting Information). Myeloid-derived phagocytic neutrophils and monocytes on the other hand extensively engaged the NEs (Figure 3d and Figure S5, Supporting Information). More specifically, M1 monocytes phagocytosed both cRGD- and cRAD-NE at high and comparable levels while neutrophils and M2 monocytes showed a significant preference for cRGD-NE over cRAD-NE (Figure 3d). Taking the shorter circulation half-life of the cRGD-NE into account (113 min vs 200 min for cRAD-NE; Figure S6, Supporting Information), this demonstrates that these phagocytes have a significant affinity for cRGD-NE, which corroborated the intravital imaging as well as the ex vivo CLSM on isolated circulatory immune cells.

To exclude NP-specific effects from our observations, additionally to the NE, we also studied ligand-conjugated LPs in vivo. Dynamic IVM during the first 30 min post-injection, although less extensively than for cRGD-NE (Movie S1, Supporting Information), showed cRGD-LP agglomerates which resembled immune cells (Movie S6, Supporting Information). The dynamic

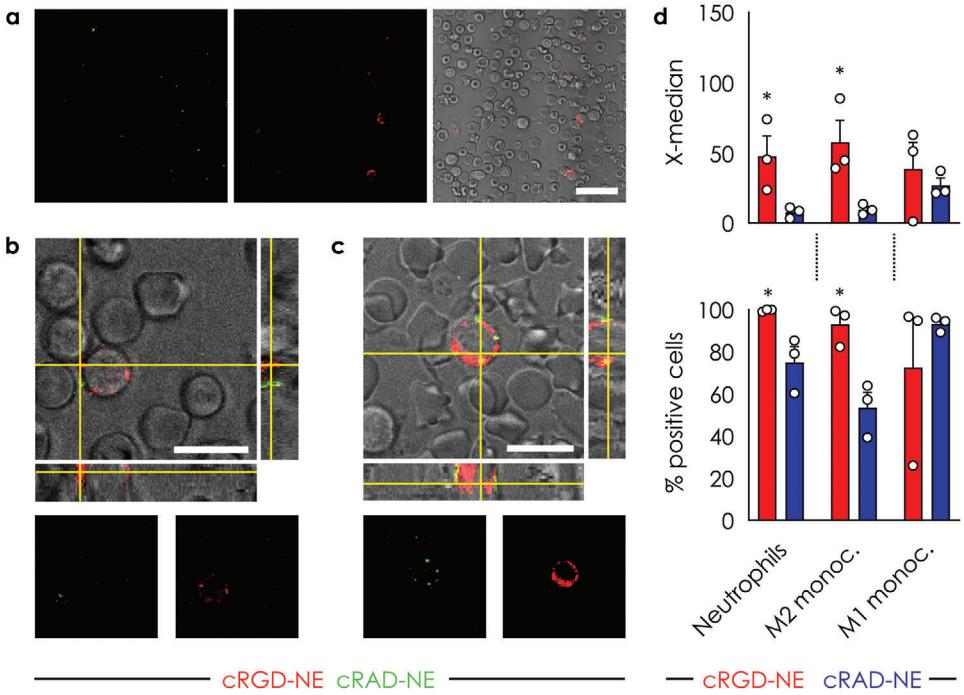

Figure 3. Ex vivo characterization of interactions between nanoemulsions and circulating immune cells. a–c) Ex vivo CLSM on immune cells isolated 5 min (a,b) and 10 min (c) post-injection of cRAD-NE (green) and cRGD-NE (red) showed that these cells associated with cRGD-NE to a much higher extent than with cRAD-NE. Cells in gray scale were imaged using transmission mode. (b) and (c) show orthogonal projections of z-stacks demonstrating the NE to be present on the cell membrane and intracellularly. d) Flow cytometry on circulating immune cells isolated 2 h after NE administration revealed myeloid-derived phagocytes to be the dominant population engaging the NE and confirmed that these cells associated with cRGD-NE to significantly higher extent than with cRAD-NE ($n = 3$; mean ± SEM). Flow cytometry histograms (Figure S5, Supporting Information) show data from representative animals revealing insignificant engagement of the NPs with lymphoid cells. Scale bars: a = 25 µm; b,c = 10 µm. *p*-values: * < 0.05.

imaging also showed binding events of 1–8 µm-sized cRGD-LP agglomerates, appearing as steps in fluorescence versus time curves (**Figure 4**a and Movie S7, Supporting Information). However, the number of binding events (14 in three mice) observed was lower than for cRGD-NE (45 in four mice). cRAD-LP gradually extravasated from the angiogenic vasculature (Figure 4b and Movie S8, Supporting Information), in line with cRAD-NE. High-speed dynamic IVM showed circulating and rolling cRGD-LP positive cells as well (Movie S9, Supporting Information). These cRGD-LP positive cells were relatively few compared to cRGD-NE up to 2 h, and most abundant at 5–6 h post-injection (Movie S9, Supporting Information). In line with the NE results, cRAD-LPs were associated with circulating phagocytes to lower extent (Movie S10, Supporting Information) and this was especially evident in co-administration experiments, which showed more cRGD-LP than cRAD-LP positive cells (Figure 4c and Movie S11, Supporting Information). Ex vivo CLSM of blood cells isolated 5, 10, and 25 min after co-administration confirmed a higher cellular uptake of cRGD-LPs than of cRAD-LPs (Figure 4d and Figure S2, Supporting Information) in accordance with the IVM data and the NE results. Utilizing the TIE2-GFP mice, we confirmed the presence of non-endothelial cell-sized cRGD-LP agglomerates bound in the vasculature at later time points (Figure 4e) and also detected the expected cRGD-LP targeting toward angiogenic endothelium (Figure 4e,f). Finally, cellular uptake of the ligand-conjugated LPs in blood cells was assessed with flow cytometry. The LP cellular uptake pattern was very similar as observed for the NE formulations (Figure 4g and Figure S5, Supporting Information), with much higher uptake of cRGD-LPs than cRAD-LPs by myeloid cells and no uptake by lymphoid cells. Considering the large difference in circulation times of the cRGD- and cRAD-LPs (115 vs 794 min, respectively, see Figure S7, Supporting Information), this confirmed the high affinity of phagocytes for cRGD-LPs.

Taken together, this study demonstrates that angiogenesis-targeting by two different lipidic cRGD-decorated NPs in inflammation is partly mediated through hitchhiking with phagocytes. We observed that circulating phagocytes specifically engaged cRGD-NPs and homed to the angiogenic endothelium. Additionally, utilizing TIE2-GFP mice, we also observed direct interactions between cRGD-NPs and angiogenic endothelium. By comparing the engagement of cRGD-NPs versus cRAD-NPs with immune cells, we observed a strong preference of neutrophils and M2 monocytes for cRGD-NPs. More than 93% of these phagocytes were found to be positive for cRGD-NPs while only 44–75% of phagocytes were positive for cRAD-NPs. With respect to M1 monocytes, almost no differences were observed in the uptake of cRGD-NPs versus cRAD-NPs. By comparing the uptake of cRGD-NEs versus cRGD-LPs by phagocytes, we only observed minor differences, with neutrophils displaying a higher preference for cRGD-LPs than for cRGD-NE. In all cases, the uptake of all the studied cRGD-NPs and cRAD-NPs by lymphoid cells was negligible. The differences in uptake between the cRGD and cRAD versions of the NE were smaller than the differences

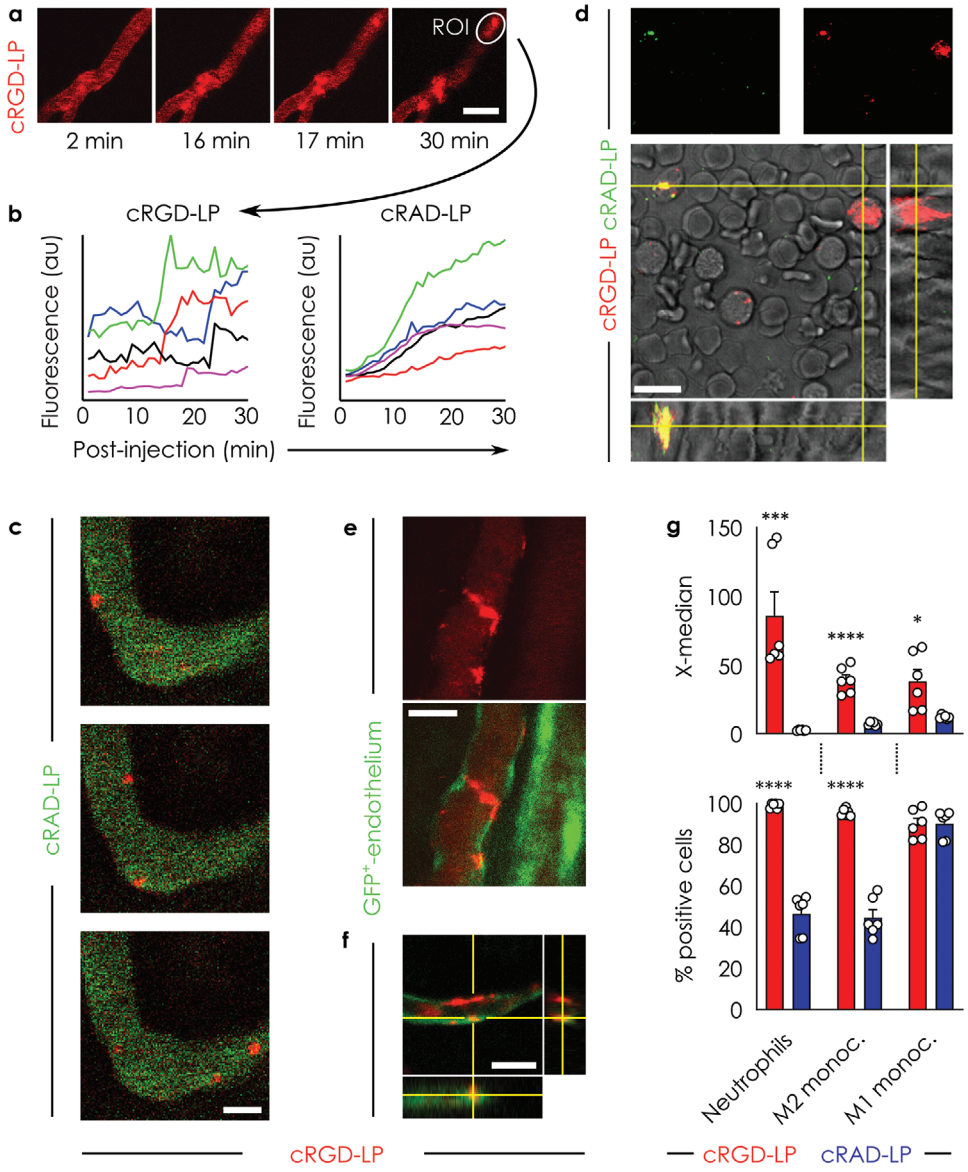

Figure 4. Inflammation endothelium targeting by cRGD-LP. a) Snapshots of a dynamic imaging series show binding events in angiogenic vasculature of cRGD-LP (red) positive cells. b) These binding events appear as "steps" in fluorescence versus time plots for cRGD-LP (each line represents ROI signal intensity of a single binding event), while cRAD-LP gradually extravasate in the inflamed tissue. c) Snapshots from high-speed imaging ($\Delta t = 1.3$ s) 20 h post co-administration of cRGD-LP (red) and cRAD-LP (green). d) Orthogonal projections of z-stacks of white blood cells isolated 25 min post cRGD-LP (red) and cRAD-LP (green) co-administration. e) 6 h post-injection, colocalization between cRGD-LP (red) and GFP positive endothelium (green) as well as non-endothelial cell-sized cRGD-LP agglomerates bound in the vasculature were observed. f) Z-stack with orthogonal projections showing cRGD-LP (red) colocalization with GFP-positive endothelium (green) at 6 h post-injection. g) Flow cytometry on blood cells isolated 2 h after cRGD-LP (red) and cRAD-LP (blue) administration, revealed myeloid cells associating with cRGD-LP to significantly higher extent than with cRAD-LP ($n = 6$; mean ± SEM). Flow cytometry histograms (Figure S5, Supporting Information) show data from representative animals and confirm that LP also engaged insignificantly with lymphoid cells. Scale bars: a,c,e = 25 µm; d,f = 10 µm. *p*-values: * < 0.05, *** < 0.001, **** < 0.0001.

between the cRGD and cRAD versions of the LPs. As evident from the significantly longer circulation half-life of the cRAD-LP as compared to cRAD-NE, cRAD-NEs were more rapidly cleared. Since clearance involves recognition by phagocytes, this could explain the relatively higher uptake of cRAD-NE as compared to the cRAD-LP in the studied phagocytic cells.

The results obtained here closely resemble the observations in one of our previous studies where we established a significant contribution of two different lipidic cRGD-NP phagocyte hitchhiking in targeting toward tumor tissue.[6] Our observations strongly suggest that phagocytes play a role in (lipidic) cRGD-NP in vivo applications in other pathological conditions as well. Interestingly, in the current study we did not observe the high extravasation propensity that phagocytes displayed in tumors. This phenomenon could be explained by the dense tissue structure in the ear[25] and the different inflammatory signaling between

cancerous and non-cancerous microenvironment.[26] Even though a thorough investigation is required to assess the biological explanation of such a difference, the high spatiotemporal resolution of IVM allows for detecting these mechanistic differences. In this regard, the use of specific antibodies can be used for the staining of specific cells and further elucidate interactions between NPs and immune cells.[27]

Several recent preclinical studies have uncovered pivotal roles for cells of the immune system in nanodrug delivery and pharmacodynamics as well. "NP hitchhiking" with neutrophils from the circulation into inflamed and malignant lesions has been observed and allowed for treatment of these conditions.[28,29] Furthermore, inflammation-associated macrophages have been demonstrated to internalize nanodrugs, migrate, and release drug payloads in tumors.[30,31] Importantly, also in human patients the interactions between nanodrugs and phagocytes can affect pharmacokinetics and pharmacodynamics.[32–35] Hence, in line with our current study, NP interactions with phagocytes can significantly affect nanodrug in vivo applications.

From a therapeutic point of view, the fact that cRGD-NPs showed a particular preference for targeting neutrophils and monocytes encourages the utilization of such nanomedicines for immune cell-specific therapeutic approaches, contributing to a paradigm shift in nanomedicine, that is, from broad organ targeting to immune cell-specific targeting.[36] The wound healing process typically involves a distinct inflammation stage in which the innate immune system is activated in response to damage-associated molecular patterns and a plethora of pro-inflammatory cytokines.[37–40] At later stages, the maintenance of inflammation results in constant activation of fibroblasts and consequently excessive deposition of scar tissue and the development of pathological fibrosis.[41] In this regard, these inflammatory and fibrotic manifestations, are typically treated by the use of small drug molecules (e.g., pirfenidone and dexamethasone) aiming to modulate inflammation/fibrosis.[42,43] The understanding that nanoformulations can target distinct myeloid cell populations involved in the wound healing/inflammation process is an important tool in our arsenal that will allow for the development of more specific and targeted therapies. In addition to the direct engagement between NPs and immune cells, by carefully observing our IVM movies we could see immune cells loaded with NPs to be in close proximity of each other (the fluorescent trait in the NPs allows for immune cell tracking). This observation reveals the strong intercellular communication that innate immune cells display in case of wound healing and inflammation.[44] Based on this notion, the robust targeting of the cRGD-NPs to myeloid cells, encourages the selection of payloads against the formation of neutrophil extracellular traps (e.g., PAD4 inhibitors), nucleotide cargo for polarizing monocytes toward an anti-inflammatory phenotype (e.g., modified messenger RNA against pro-inflammatory cytokine expression), or the development of gene editing systems for stimulating the production of anti-inflammatory cytokines.[45–47] These latter suggested examples highlight state-of-the-art therapeutic concepts that will potentially benefit greatly from immune cell-specific-targeting in the context of wound healing and inflammation, and promote strategies for interrupting the pro-inflammatory cascade. In this regard, and depending on the disease-target, different nanomaterials functionalized with RGD or other peptides may enable to shift the targeting specificity among the various myeloid cell populations.[6,48]

Although our study is limited to cRGD, the spectacular preclinical results and limited clinical applicability of ligand-decorated nanomedicine in general[49] underlines the pressing need for improved understanding of "NP real-time in vivo behavior." In the current study, the dynamic IVM was pivotal to arrive at the realization that phagocytes contribute to cRGD-NP targeting of angiogenic endothelium on the wound-healing model and to reveal similarities and differences in the contribution of phagocytes in cRGD-NP targeting in tumors (no such patterns were observed in case of healthy endothelium targeting).[6] Moreover, utilizing a mouse model with endothelial GFP expression allowed us to observe direct (although limited) interactions between cRGD-NPs and endothelial cells in vivo and to discriminate between endothelial cells and immune cells accumulating along the vessel wall. Hence, IVM approaches in combination with stable fluorescent labeling of specific cell types, not only endothelial cells as we employed here, but, for example, also tumor cells or various myeloid cells,[50–52] will allow unraveling NP cell interactions in vivo at necessary and unprecedented detail. Together with more detailed knowledge on parameters like nanodrug pharmacodynamics, targeting kinetics, and in vivo drug release profiles, IVM can be an instrumental tool to gain critically needed insights in NP in vivo behavior.[21,33,53–55]

3. Conclusion

We demonstrated that in vivo targeting of cRGD-NPs toward inflamed lesions is a result of two distinct processes; direct cRGD-NP binding to the activated endothelial cells, as well as "phagocyte hitchhiking" to the endothelium. Interestingly, these processes closely resemble the targeting mechanisms of these NPs toward the tumor vasculature and microenvironment. This insight complicates in vivo application of cRGD-NPs for their conventional purpose of angiogenesis targeting. To allow for rational cRGD-NP application, these insights necessitate a detailed characterization to quantify the contribution of each of the two modes of lesion targeting. Since successful clinical utilization of drug delivery systems depends on a thorough insight into pharmacokinetics, pharmacodynamics, and targeting mechanisms, this study underlines the pressing need for an improved understanding of NP in vivo behavior.

4. Experimental Section

Nanoparticle Synthesis: NEs and LPs were prepared according to established methods.[53] A total of 20 µmol of lipids, that is, DSPC, cholesterol, and maleimide-PEG2000-DSPE (Avanti Polar Lipids) were dissolved and mixed in chloroform at molar ratios of 0.62:0.33:0.05. For fluorescent NP detection, 0.2 mol % of Atto633-PE (Sigma Aldrich) or rhodamine-PE (Avanti Polar Lipids) was added in the mix. In case of NE, an amount of 2.5 mg of soybean oil (Sigma Aldrich) per µmol of lipid was added in the chloroform mix as well. The mixture was added dropwise to 2 mL hepes buffered saline (HBS), which was maintained at 75 °C and vigorously stirred, upon which the chloroform evaporated. The obtained formulations were downsized with a tip-sonicator (Heat Systems-Ultrasonics) via established protocols.[6] Half of the final NP formulation was conjugated with cRGD peptide (Peptides International, PCI-3699-PI) and the other half with control cRAD peptide (Peptides International, PCI-3959-PI) at 13.5 µg

per µmol lipid. Before adding cRGD or cRAD peptides to the maleimide-containing NPs, the thiol on the peptides was de-acetylated (pH 7, 1 h). The activated peptides were left to react with the NPs overnight at 4 °C. Finally, the NPs were dialyzed against HBS of pH 7.4 and stored at 4 °C for a minimum of 5 days for complete hydrolysis of unreacted maleimide moieties. The obtained LPs and NEs were around 90 and 120 nm in hydrodynamic diameter, respectively, with dispersity below 0.15 (Figure S1, Supporting Information) as determined with dynamic light scattering (Zetasizer, Malvern).

Mice: Immunocompetent Balb/c mice (Envigo) were used for the in vivo IVM and ex vivo flow cytometry experiments. Additionally, to study direct endothelial cell targeting, two STOCK Tg(TIE2GFP)287Sato/J mice (strain 003658, The Jackson Laboratory, bred in-house) were included in each experimental group in the IVM experiments. The vascular endothelial cells of these mice express GFP. Mice were kept under pathogen-free conditions, at 19–22 °C, and 50–60% humidity, and they were allowed food and water ad libitum. All experiments were approved by the national regulatory authority (Norwegian Food Safety Authorities). The mice were anesthetized (fentanyl [0.05 mg kg^{-1}], medetomidine [0.5 mg kg^{-1}], midazolam [0.5 mg kg^{-1}], and water; 2:1:2:5 ratio) by a 0.2–0.25 mL subcutaneous injection.

Measurement of Nanoparticle Circulation Half-Lives: To determine NP circulation half-lives, mice were anesthetized and i.v. injected with a NP bolus (80 µmol of amphiphilic lipid/kg, $n = 3$ per formulation, cRGD- or cRAD-NE and LP). At 5, 30 min, 1, 2, 4, 8, and 24 h post-injection a blood drop (≈10 µL) was collected from the tail-vein into preweighted centrifuge tubes containing 20 µL heparin at 1 IU/mL 0.9% NaCl. The tubes were weighed for registering the collected blood volume and centrifuged at 700 g for 8 min. The fluorescence in the collected supernatant plasma was quantified with a spectrophotometer (SpectraMax i3x, Molecular Devices). The obtained data was fitted with the curve fitting tool in Matlab.

Intravital Microscopy: A 3–4 mm cut was inflicted in the mouse ear and after 2 days NP targeting toward angiogenic vasculature present in the wound healing process was studied. Mice were anesthetized and to allow IVM, hair was removed with hair removal cream and the ear was submerged in a drop of glycerol on a cover slip and fixed gently with tape. Mice were cannulated in the tail-vein and placed on a microscopy stage with monitored temperature. Directly after i.v. administration of a NP bolus (80 µmol of lipid/kg, $n = 4$ for NE, and $n = 3$ for LP), the detector gain and laser power of the microscope were adjusted accordingly, and from 60–120 s post-injection the mice were imaged dynamically (temporal resolution 1 min) for ≈30 min to assess NP targeting kinetics. Moreover, high-speed imaging (temporal resolution: 0.3–2 s) was employed in order to investigate the uptake of NPs by circulating immune cells at various time points, and the authors collected additional static images and z-stacks up to 24 h post-injection. In addition to the injection of a single NP per mouse, mice were co-injected with cRGD-NP and cRAD-NP (labeled with Atto633 or rhodamine) in order to investigate differences between the two formulations ($n = 2$ for NE and $n = 2$ for LP). Intravital CLSM was performed on a Leica SP8 system, and the images were acquired with a 20×/0.95 air objective. For the various used fluorophores, the following combinations of excitation and detection wavelengths were used: GFP (488 nm/500–515 nm), rhodamine (560 nm/570–600 nm), and Atto633 (633 nm/645–700)

Ex Vivo Confocal Laser Scanning Microscopy: For corroborating the authors' in vivo findings, ex vivo CLSM was performed on isolated immune cells. Mice were co-injected with cRGD-NPs and cRAD-NPs (labeled with Atto633 or rhodamine) and blood (≈1 mL) was collected via heart puncturing at 5, 10, and 25 min post-injection. The collected blood was immediately placed in 1 mL heparin (1 IU/mL in 0.9% NaCl). The white blood cells were isolated via a density gradient method (Lymphoprep; Nycomed Pharma), they were transferred in wells, and directly imaged with the same settings as the IVM and a 40×/1.1 water objective.

Ex Vivo Flow Cytometry on Blood: For ex vivo flow cytometry experiments, mice were anesthetized and i.v. injected with a NP bolus (80 µmol of lipid/kg, $n = 3$ for cRGD-NE, $n = 3$ for cRAD-NE, $n = 6$ for cRGD-LP, and $n = 6$ for cRAD-LP). Right after NP administration, all mice subcutaneously received 0.2–0.25 mL antidote (atipemazol [2.5 mg kg^{-1}], flumazenil [0.5 mg kg^{-1}], and water; 1:1:8 ratio) for completely reversing the anesthesia. At 2 h post-injection, mice were sacrificed and blood (≈1 mL) was collected via heart puncturing and placed in a heparinized blood collection tube. The red blood cell lysis was performed according to established protocols and the obtained immune cells were resuspended in 0.5 mL PBS supplemented with 2% FCS and 2 mM EDTA (FACS buffer).[6] The dispersion was incubated with 5.0 µg anti-mouse CD16/32 (TruStain fcX) for 10 min on ice. Then, samples of 0.1 mL were incubated with an antibody cocktail for 30 min on ice in the dark (antibody cocktail: Brilliant Violet 421 anti-CD11b [2 µL], Brilliant Violet 510 anti-Ly6G [2 µL], and PE/Cy7 anti-CD19 [1.5 µL], and APC-eFluor 780 anti-CD3e [2.5 µL]). The cells were washed with FACS buffer via two rounds of centrifugation (400 g, 5 min), and resuspended in final volume of 200 µL FACS buffer. As last step, 1 µL of 7-aminoactinomycin D (7-AAD) live/dead marker was added in this sample. The flow cytometry procedure was performed using a Gallios (Beckman Coulter) cytometer and for each sample 100k total counts were collected. The following excitation wavelengths and detection bandpass filters were used: Brilliant Violet 421 (405 nm/450/50 nm), Brilliant Violet 510 (405 nm/550/40 nm), 7-AAD (488 nm/620/30 nm), PE/Cy7 (488 nm/755LP nm), Atto633 (633 nm/660/20 nm), and APC-eFluor780 (633 nm/755LP nm). Samples with single colors were run under the same laser voltage and gain conditions to ensure proper compensation. During the analysis, the cellular fragments and debris were excluded (appearing as low forward and side scatter signals), and the dead cells were excluded based on the high 7-AAD signal.

Statistical Analysis and Software: The obtained CLSM images, z-stacks, and videos were analyzed and prepared for publication using ImageJ and the graphs were plotted with Matlab. The flow cytometry data were analyzed with Kaluza software (Beckman Coulter). The graphs were plotted in GraphPad Prism 9 as mean ± SEM ($n = 3$ for cRGD-NE, $n = 3$ for cRAD-NE, $n = 6$ for cRGD-LP, and $n = 6$ for cRAD-LP) and two population comparisons were conducted with a two-tailed *t*-test. The significances were determined by the received *p*-values: * ≤ 0.05, ** ≤ 0.01, *** ≤ 0.001, and **** ≤ 0.0001.

Supporting Information

Supporting Information is available from the Wiley Online Library or from the author.

Acknowledgements

This work was supported by the Central Norway Regional Health Authority "Helse Midt-Norge" (A.M.S.: Ph.D. stipend [90062100] and travel grant [90284100]; S.H.: researcher grant [90262100]), the Norwegian Research Council (S.H.: 230788/F20), the Tromsø Research Foundation, and Trond Mohn Foundation (S.H.: 180°N project).

Conflict of Interest

JO and WJMM are scientific founders of Trained Therapeutix Discovery.

Data Availability Statement

Data available on request from the authors

Keywords

arginine–glycine–aspartate, immunotherapy, inflammation, intravital microscopy, nanomedicines, neutrophils, phagocyte hitchhiking

Received: January 28, 2021
Revised: March 5, 2021
Published online: May 3, 2021

[1] D. Schmid, C. G. Park, C. A. Hartl, N. Subedi, A. N. Cartwright, R. B. Puerto, Y. Zheng, J. Maiarana, G. J. Freeman, K. W. Wucherpfennig, D. J. Irvine, M. S. Goldberg, *Nat. Commun.* **2017**, *8*, 1747.
[2] R. Kedmi, N. Veiga, S. Ramishetti, M. Goldsmith, D. Rosenblum, N. Dammes, I. Hazan-Halevy, L. Nahary, S. Leviatan-Ben-Arye, M. Harlev, M. Behlke, I. Benhar, J. Lieberman, D. Peer, *Nat. Nanotechnol.* **2018**, *13*, 214.
[3] C. B. Rodell, S. P. Arlauckas, M. F. Cuccarese, C. S. Garris, R. Li, M. S. Ahmed, R. H. Kohler, M. J. Pittet, R. Weissleder, *Nat. Biomed. Eng.* **2018**, *2*, 578.
[4] F. Combes, E. Meyer, N. N. Sanders, *J. Controlled Release* **2020**, *327*, 70.
[5] A. M. Sofias, T. Andreassen, S. Hak, *Mol. Pharmaceutics* **2018**, *15*, 5754.
[6] A. M. Sofias, Y. C. Toner, A. E. Meerwaldt, M. M. T. van Leent, G. Soultanidis, M. Elschot, H. Gonai, K. Grendstad, Å. Flobak, U. Neckmann, C. Wolowczyk, E. L. Fisher, T. Reiner, C. de L. Davies, G. Bjørkøy, A. J. P. Teunissen, J. Ochando, C. Pérez-Medina, W. J. M. Mulder, S. Hak, *ACS Nano* **2020**, *14*, 7832.
[7] J. Hou, X. Yang, S. Li, Z. Cheng, Y. Wang, J. Zhao, C. Zhang, Y. Li, M. Luo, H. Ren, J. Liang, J. Wang, J. Wang, J. Qin, *Sci. Adv.* **2019**, *5*, eaau8301.
[8] Z. Chen, A. Bozec, A. Ramming, G. Schett, *Nat. Rev. Rheumatol.* **2019**, *15*, 9.
[9] G. A. Robinson, J. Peng, P. Dönnes, L. Coelewij, M. Naja, A. Radziszewska, C. Wincup, H. Peckham, D. A. Isenberg, Y. Ioannou, I. Pineda-Torra, C. Ciurtin, E. C. Jury, *Lancet Rheumatol.* **2020**, *2*, e485.
[10] T. Binderup, R. Duivenvoorden, F. Fay, M. M. T. van Leent, J. Malkus, S. Baxter, S. Ishino, Y. Zhao, B. Sanchez-Gaytan, A. J. P. Teunissen, Y. C. A. Frederico, J. Tang, G. Carlucci, S. Lyashchenko, C. Calcagno, N. Karakatsanis, G. Soultanidis, M. L. Senders, P. M. Robson, V. Mani, S. Ramachandran, M. E. Lobatto, B. A. Hutten, J. F. Granada, T. Reiner, F. K. Swirski, M. Nahrendorf, A. Kjaer, E. A. Fisher, Z. A. Fayad, C. Pérez-Medina, W. J. M. Mulder, *Sci. Transl. Med.* **2019**, *11*, eaaw7736.
[11] M. S. Braza, M. M. T. van Leent, M. Lameijer, B. L. Sanchez-Gaytan, R. J. W. Arts, C. Pérez-Medina, P. Conde, M. R. Garcia, M. Gonzalez-Perez, M. Brahmachary, F. Fay, E. Kluza, S. Kossatz, R. J. Dress, F. Salem, A. Rialdi, T. Reiner, P. Boros, G. J. Strijkers, C. C. Calcagno, F. Ginhoux, I. Marazzi, E. Lutgens, G. A. F. Nicolaes, C. Weber, F. K. Swirski, M. Nahrendorf, E. A. Fisher, R. Duivenvoorden, Z. A. Fayad, M. G. Netea, W. J. M. Mulder, J. Ochando, *Immunity* **2018**, *49*, 819.
[12] C. Rosales, *Front. Physiol.* **2018**, *9*, 113.
[13] S. Sindhwani, A. M. Syed, J. Ngai, B. R. Kingston, L. Maiorino, J. Rothschild, P. MacMillan, Y. Zhang, N. U. Rajesh, T. Hoang, J. L. Y. Wu, S. Wilhelm, A. Zilman, S. Gadde, A. Sulaiman, B. Ouyang, Z. Lin, L. Wang, M. Egeblad, W. C. W. Chan, *Nat. Mater.* **2020**, *19*, 566.
[14] Y. Matsumoto, J. W. Nichols, K. Toh, T. Nomoto, H. Cabral, Y. Miura, R. J. Christie, N. Yamada, T. Ogura, M. R. Kano, Y. Matsumura, N. Nishiyama, T. Yamasoba, Y. H. Bae, K. Kataoka, *Nat. Nanotechnol.* **2016**, *11*, 533.
[15] I. Biancacci, Q. Sun, D. Möckel, F. Gremse, S. Rosenhain, F. Kiessling, M. Bartneck, Q. Hu, M. Thewissen, G. Storm, W. E. Hennink, Y. Shi, C. J. F. Rijcken, T. Lammers, A. M. Sofias, *J. Controlled Release* **2020**, *328*, 805.
[16] J. S. de Maar, A. M. Sofias, T. P. Siegel, R. J. Vreeken, C. Moonen, C. Bos, R. Deckers, *Theranostics* **2020**, *10*, 1884.
[17] A. M. Sofias, A. K. O. Åslund, N. Hagen, K. Grendstad, S. Hak, *Mol. Imaging Biol.* **2020**, *22*, 486.
[18] A. Rege, N. V. Thakor, K. Rhie, A. P. Pathak, *Angiogenesis* **2012**, *15*, 87.
[19] M. G. Tonnesen, X. Feng, R. A. F. Clark, *J. Invest. Dermatol. Symp. Proc.* **2000**, *5*, 40.
[20] T. Ojha, V. Pathak, Y. Shi, W. E. Hennink, C. T. W. Moonen, G. Storm, F. Kiessling, T. Lammers, *Adv. Drug Delivery Rev.* **2017**, *119*, 44.
[21] S. Hak, J. Cebulla, E. M. Huuse, C. de L. Davies, W. J. M. Mulder, H. B. W. Larsson, O. Haraldseth, *Angiogenesis* **2014**, *17*, 93.
[22] G. J. Strijkers, S. Hak, M. B. Kok, C. S. Springer, K. Nicolay, *Magn. Reson. Med.* **2009**, *61*, 1049.
[23] M. B. Kok, S. Hak, W. J. M. Mulder, D. W. J. van der Schaft, G. J. Strijkers, K. Nicolay, *Magn. Reson. Med.* **2009**, *61*, 1022.
[24] J. A. Nemzek, G. L. Bolgos, B. A. Williams, D. G. Remick, *Inflammation Res.* **2001**, *50*, 523.
[25] R. J. Kerschbaumer, M. Rieger, D. Völkel, D. Le Roy, T. Roger, J. Garbaraviciene, W.-H. Boehncke, J. Müllberg, R. M. Hoet, C. R. Wood, G. Antoine, M. Thiele, H. Savidis-Dacho, M. Dockal, H. Ehrlich, T. Calandra, F. Scheiflinger, *J. Biol. Chem.* **2012**, *287*, 7446.
[26] S. A. C. McDowell, D. F. Quail, *Front. Immunol.* **2019**, *10*, 1984.
[27] V. A. Naumenko, S. S. Vodopyanov, K. Y. Vlasova, D. M. Potashnikova, P. A. Melnikov, D. A. Vishnevskiy, A. S. Garanina, M. P. Valikhov, A. V. Lipatova, V. P. Chekhonin, A. G. Majouga, M. A. Abakumov, *J. Controlled Release* **2021**, *330*, 244.
[28] D. Chu, J. Gao, Z. Wang, *ACS Nano* **2015**, *9*, 11800.
[29] D. Chu, Q. Zhao, J. Yu, F. Zhang, H. Zhang, Z. Wang, *Adv. Healthcare Mater.* **2016**, *5*, 1088.
[30] M. L. Senders, A. E. Meerwaldt, M. M. T. van Leent, B. L. Sanchez-Gaytan, J. C. van de Voort, Y. C. Toner, A. Maier, E. D. Klein, N. A. T. Sullivan, A. M. Sofias, H. Groenen, C. Faries, R. S. Oosterwijk, E. M. van Leeuwen, F. Fay, E. Chepurko, T. Reiner, R. Duivenvoorden, L. Zangi, R. M. Dijkhuizen, S. Hak, F. K. Swirski, M. Nahrendorf, C. Pérez-Medina, A. J. P. Teunissen, Z. A. Fayad, C. Calcagno, G. J. Strijkers, W. J. M. Mulder, *Nat. Nanotechnol.* **2020**, *15*, 398.
[31] C. W. Shields, M. A. Evans, L. L.-W. Wang, N. Baugh, S. Iyer, D. Wu, Z. Zhao, A. Pusuluri, A. Ukidve, D. C. Pan, S. Mitragotri, *Sci. Adv.* **2020**, *6*, eaaz6579.
[32] W.-C. Huang, S.-H. Chen, W.-H. Chiang, C.-W. Huang, C.-L. Lo, C.-S. Chern, H.-C. Chiu, *Biomacromolecules* **2016**, *17*, 3883.
[33] M. A. Miller, Y.-R. Zheng, S. Gadde, C. Pfirschke, H. Zope, C. Engblom, R. H. Kohler, Y. Iwamoto, K. S. Yang, B. Askevold, N. Kolishetti, M. Pittet, S. J. Lippard, O. C. Farokhzad, R. Weissleder, *Nat. Commun.* **2015**, *6*, 8692.
[34] H. Giovinazzo, P. Kumar, A. Sheikh, K. M. Brooks, M. Ivanovic, M. Walsh, W. P. Caron, R. J. Kowalsky, G. Song, A. Whitlow, D. L. Clarke-Pearson, W. R. Brewster, L. Van Le, B. A. Zamboni, V. Bae-Jump, P. A. Gehrig, W. C. Zamboni, *Cancer Chemother. Pharmacol.* **2016**, *77*, 565.
[35] G. Song, J. Petschauer, A. Madden, W. Zamboni, *Curr. Rheumatol. Rev.* **2014**, *10*, 22.
[36] A. M. Sofias, F. Combes, S. Koschmieder, G. Storm, T. Lammers, *Drug Discovery Today* **2021**, https://doi.org/10.1016/j.drudis.2021.02.017.
[37] T. J. Koh, L. A. DiPietro, *Expert Rev. Mol. Med.* **2011**, *13*, e23.
[38] J. V. Dovi, L.-K. He, L. A. DiPietro, *J. Leukocyte Biol.* **2003**, *73*, 448.
[39] A. Sindrilaru, T. Peters, S. Wieschalka, C. Baican, A. Baican, H. Peter, A. Hainzl, S. Schatz, Y. Qi, A. Schlecht, J. M. Weiss, M. Wlaschek, C. Sunderkötter, K. Scharffetter-Kochanek, *J. Clin. Invest.* **2011**, *121*, 985.
[40] S. Barrientos, O. Stojadinovic, M. S. Golinko, H. Brem, M. Tomic-Canic, *Wound Repair Regener.* **2008**, *16*, 585.
[41] T. J. Keane, C. M. Horejs, M. M. Stevens, *Adv. Drug Delivery Rev.* **2018**, *129*, 407.
[42] A. Mortensen, L. Cherrier, R. Walia, *Multidiscip. Respir. Med.* **2018**, *13*, 16.
[43] A. S. Wang, E. J. Armstrong, A. W. Armstrong, *Am. J. Surg.* **2013**, *206*, 410.
[44] A. Rivera, M. C. Siracusa, G. S. Yap, W. C. Gause, *Nat. Immunol.* **2016**, *17*, 356.
[45] N. Veiga, M. Goldsmith, Y. Granot, D. Rosenblum, N. Dammes, R. Kedmi, S. Ramishetti, D. Peer, *Nat. Commun.* **2018**, *9*, 4493.
[46] O. Tatsiy, P. P. McDonald, *Front. Immunol.* **2018**, *9*, 2036.
[47] E. Sloane, A. Ledeboer, W. Seibert, B. Coats, M. van Strien, S. F. Maier, K. W. Johnson, R. Chavez, L. R. Watkins, L. Leinwand, E. D. Milligan, A. M. Van Dam, *Brain, Behav., Immun.* **2009**, *23*, 92.

[48] B. R. Smith, E. E. B. Ghosn, H. Rallapalli, J. A. Prescher, T. Larson, L. A. Herzenberg, S. S. Gambhir, *Nat. Nanotechnol.* **2014**, *9*, 481.
[49] D. Witzigmann, S. Hak, R. van der Meel, *J. Controlled Release* **2018**, *290*, 138.
[50] A. Leimgruber, C. Berger, V. Cortez-Retamozo, M. Etzrodt, A. P. Newton, P. Waterman, J. L. Figueiredo, R. H. Kohler, N. Elpek, T. R. Mempel, F. K. Swirski, M. Nahrendorf, R. Weissleder, M. J. Pittet, *Neoplasia* **2009**, *11*, 459.
[51] A. Bartocci, D. S. Mastrogiannis, G. Migliorati, R. J. Stockert, A. W. Wolkoff, E. R. Stanley, J. Smith, Z. Werb, *Proc. Natl. Acad. Sci. USA* **1987**, *84*, 6179.
[52] J. F. Mohan, R. H. Kohler, J. A. Hill, R. Weissleder, D. Mathis, C. Benoist, *Proc. Natl. Acad. Sci. USA* **2017**, *114*, E7776.
[53] S. Hak, E. Helgesen, H. H. Hektoen, E. M. Huuse, P. A. Jarzyna, W. J. M. Mulder, O. Haraldseth, C. de L. Davies, *ACS Nano* **2012**, *6*, 5648.
[54] Y. Zhao, F. Fay, S. Hak, J. M. Perez-Aguilar, B. L. Sanchez-Gaytan, B. Goode, R. Duivenvoorden, C. de L. Davies, A. Bjørkøy, H. Weinstein, Z. A. Fayad, C. Pérez-Medina, W. J. M. Mulder, *Nat. Commun.* **2016**, *7*, 11221.
[55] Y. Zhao, I. van Rooy, S. Hak, F. Fay, J. Tang, C. de L. Davies, M. Skobe, E. A. Fisher, A. Radu, Z. A. Fayad, C. de Mello Donegá, A. Meijerink, W. J. M. Mulder, *ACS Nano* **2013**, *7*, 10362.

